

Nonlinear Dynamics of an Oscillator Inductively Coupled to an External Resonator for Power Transfer and Data Transmission

Víctor Ardila^{ID}, *Student Member, IEEE*, Franco Ramírez^{ID}, *Senior Member, IEEE*,
and Almudena Suárez^{ID}, *Fellow, IEEE*

Abstract—This work presents an investigation of the nonlinear dynamics of an oscillator that is inductively coupled to an external resonator for power transfer applications. Analytical expressions are derived for the oscillation frequency and output power, which provide insight into the effect of the coupled resonator on the oscillator solution. From the analytical study, criteria are derived to maximize the k range with a high efficiency and a limited variation of the oscillation frequency. The resistor of the external resonator can be modulated for data transmission to the core oscillator. Here the sensitivity to this resistor and its dependence on the coupling factor are analyzed in detail. The methods have been applied to a Class-E oscillator that has been analyzed through a contour-intersection technique. This is based on the extraction from harmonic balance (HB) of a bi-variate nonlinear admittance function accounting for the oscillator circuit, which is combined with the passive linear admittance function of the coupled resonator. The advantage is taken of the ease of this analysis to obtain constant-efficiency contours in the oscillatory regime, traced in the plane defined by the coupling factor and any suitable analysis parameter. By means of a bifurcation analysis, various phenomena, including the oscillation extinction plus onset versus the coupling factor and the appearance of quasi-periodic solutions, are detected and avoided. Very good correspondence has been obtained between simulation and measured results.

Index Terms—Bifurcation, inductive coupling, nonlinear circuit analysis, oscillator.

I. INTRODUCTION

SHORT-DISTANCE wireless power transfer can be applied to recharge sensor networks, implantable devices, electrical car batteries, and other systems [1], [2]. To obtain high efficiency, a Class-E amplifier inductively coupled to an external resonator is often used on the primary side [3]. However, this requires a suitable drive signal, which complicates the design and reduces the power-added efficiency. This limitation can

Manuscript received July 21, 2021; revised October 25, 2021; accepted December 16, 2021. This work was supported in part by the Spanish Ministry of Science and Innovation and in part by the European Regional Development Fund (MCIN/AEI /10.13039/501100011033/ERDF “A Way of Making Europe”) under Grant TEC2017-88242-C3-1-R and Grant PID2020-116569RB-C31. This article is an expanded version from the 2021 IEEE MTT-S International Microwave Symposium (IMS 2021). (Corresponding author: Franco Ramírez.)

The authors are with the Departamento de Ingeniería de Comunicaciones, Universidad de Cantabria, 39005 Santander, Spain (e-mail: victorangel.ardila@unican.es; ramirezf@unican.es; suareza@unican.es).

Color versions of one or more figures in this article are available at <https://doi.org/10.1109/TMTT.2021.3138074>.

Digital Object Identifier 10.1109/TMTT.2021.3138074

be overcome through the implementation of a high-efficiency oscillator [3]–[13] as this allows the autonomous generation of the excitation signal. As in the amplifier case, the loading conditions depend on the coupling factor between the transmit and receive coils, which may significantly degrade the transfer efficiency. The works [7], [13] optimize the oscillator design for a given distance between the coils, while [5], [8], [12], [14] perform this optimization considering the variation of the oscillator equivalent load. With a different goal, [15] focuses on the global behavior of the inductively coupled oscillator versus variations in the coupling factor k . Using a simplified expression of the oscillator equivalent load, [15] presents an analytical study that allows the derivation of a compact relationship between the oscillation amplitude and k . However, the formulation in [15] cannot reliably predict the variation with k of the oscillation frequency, which is an essential characteristic of the coupled-oscillator solution. Moreover, the simplifying assumptions in [15] prevent the prediction of relevant phenomena such as the extinction and onset of the oscillation when increasing k , and the appearance of doubly autonomous quasi-periodic solutions, observed experimentally.

This work expands and generalizes the analytical investigation in [15] by considering the full dependence of the oscillator load on the coupling factor k , which will demand judicious derivations to get insightful results. Using these general expressions, we will analyze the impact of the k -dependent load admittance on the startup conditions and steady-state oscillation. This will allow predicting the variation with k of the oscillation frequency, which may lead the system out of the regulated frequency bands. Departing from a cubic nonlinearity oscillator, we will demonstrate that the normalized oscillation frequency is governed by a bi-cubic equation solely depending on k and the quality factor of the coupled resonator. Criteria will be derived to maximize the k range with a high efficiency and a limited variation of the oscillation frequency. Note that a suitable behavior in a sufficiently large k interval is necessary even at short distances because of possible misalignments between the coils [16]. As proposed in [17]–[20], the external resonator can be modulated for data transmission purposes. Here the modulated behavior will be analyzed with an envelope transient [21]–[23] formulation. The aim will be to maximize the oscillator sensitivity to the load modulation considering its dependence on k ,

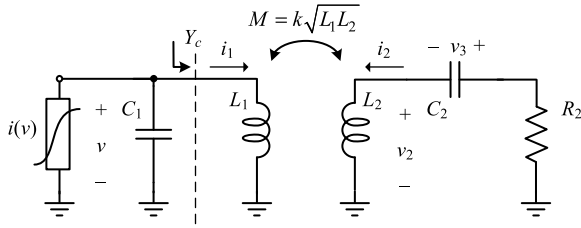


Fig. 1. Simple oscillator used in the analytical study: $C_1 = C_2 = 9.7$ pF, $L_1 = 5.6$ nH, $R_2 = 30$ Ω , $i(v) = av + bv^3$ ($a = -0.01$ A/V and $b = 0.01$ A/V³).

or equivalently, on the distance between the oscillator and the resonator.

After this analytical study, a practical Class-E oscillator will be analyzed, focusing on the impact of the coupling on the oscillator solution and its dynamics. Among other new techniques, a graphical procedure for a quick global evaluation of the oscillation startup conditions in terms of the coupling factor and element values of the external resonator is presented. For the steady-state analysis, the core oscillator is described with a numerical bi-variate nonlinear admittance function, depending on the frequency and amplitude at the coupled-inductor terminals, which is extracted from harmonic balance (HB). In turn, the coupling to the external resonator is described analytically. This way, and under any variation in the external resonator and/or coupling conditions, one can predict the system behavior with no need to perform a new HB oscillator analysis, often exhibiting convergence problems, as will be shown here. Taking advantage of the ease of this oscillator analysis, a new method is proposed to derive constant-efficiency contours in the oscillatory regime for the first time to our knowledge. A bifurcation detection technique will allow predicting and avoiding various phenomena, including the oscillation extinction and the appearance of quasi-periodic solutions. The inductively coupled oscillator has been manufactured and experimentally characterized to validate the analysis results.

The article is organized as follows. Section II presents an analytical study of a coupled system based on a cubic-nonlinearity oscillator. Section III describes the transistor-based oscillator, considering the startup conditions, steady-state operation, oscillation boundaries, constant-efficiency contours, and modulated behavior.

II. ANALYTICAL STUDY OF THE FREE-RUNNING OSCILLATOR

The initial analytical study will be based on the cubic nonlinearity oscillator in Fig. 1, inductively coupled to a passive resonator. We have considered a parallel-resonator oscillator coupled to a series external resonator. However, the analysis methodology can be extended to other topologies in a straightforward manner. The coupled system will be analyzed at the fundamental frequency using the describing function [24]. As will be shown in Section III, the main results of this study are applicable to practical oscillators described with an outer-tier admittance function extracted from HB, due to their output filtering effects.

When coupled to the external resonator, the steady-state oscillation at the frequency ω fulfills the complex equation

$$Y_T(V, \omega, k) = a + \frac{3}{4}bV^2 + jC_1\omega + Y_c(k, \omega) \quad (1)$$

where $a < 0$ and $b > 0$ and $Y_c(k, \omega)$ is the coupled admittance, seen from the oscillator coupled inductor (including this inductor), as shown in Fig. 1. This admittance is

$$Y_c(\omega, k) = \frac{1}{jL_1\omega + \frac{jk^2L_1L_2C_2\omega^3}{1-L_2C_2\omega^2 + jR_2C_2\omega}}. \quad (2)$$

In the work [15], we had performed a Taylor series expansion of Y_c about $k = 0$, which provided the expressions

$$Y_{T,r}(V, \omega, k) \cong a + \frac{3}{4}bV^2 + \frac{1}{L_1} \frac{k^2L_2R_2C_2^2\omega^2}{(1-L_2C_2\omega^2)^2 + (R_2C_2\omega)^2} = 0 \quad (3a)$$

$$Y_{T,i}(\omega, k) \cong C_1\omega - \frac{1}{L_1\omega} + \frac{1}{L_1} \frac{k^2L_2C_2\omega(1-L_2C_2\omega^2)}{(1-L_2C_2\omega^2)^2 + (R_2C_2\omega)^2} = 0 \quad (3b)$$

where the subscripts r and i indicate real and imaginary parts. The approximation (3a) facilitates the analysis of the coupled system but fails to predict relevant effects observed for intermediate and high k values. For example, when the external resonator frequency agrees with the standalone oscillation frequency $\omega_o = 1/(L_1C_1)^{1/2} = 1/(L_2C_2)^{1/2}$, (3b) provides $\omega = \omega_o$ for all the k values. However, this will only be true for relatively small k . Here, the full expression of the coupled admittance $Y_c(k, \omega)$ will be considered, which due to its complexity, will demand judicious derivations to obtain insightful results.

A. Oscillation Startup Conditions

We will first consider the imaginary part of the complex equation in (1). This provides the following real equation:

$$Y_{T,i}(\omega) = C_1\omega + Y_{c,i}(k, \omega) = C_1\omega - \frac{L_1L_2^2C_2^2(1-k^2)\omega^5}{\left[L_1C_2^2R_2^2 + L_1L_2C_2(k^2-2) \right] \omega^3 + L_1\omega} = 0. \quad (4)$$

Note that at $k = 0$, equation (4) becomes the standalone resonance condition $Y_{T,i} = C_1\omega - 1/(L_1\omega) = 0$. In general, to maximize the coupling effects [25] one should have $\omega_o = 1/(L_1C_1)^{1/2} = 1/(L_2C_2)^{1/2}$. Assuming this condition, we will transform (4) into a manageable expression by defining a normalized oscillation frequency $\gamma = \omega/\omega_o$ and making use of the quality factor Q_2 of the external resonator, given by $Q_2 = 1/(R_2C_2\omega_o)$. Introducing both expressions in (4) and performing some manipulations, one obtains

$$f(\gamma, k, Q_2) = (k^2 - 1)^2\gamma^6 + [3(k^2 - 1) + Q_2^{-2}]\gamma^4 + [3 - Q_2^{-2} - k^2]\gamma^2 - 1 = 0. \quad (5)$$

The equation (5), which is bi-cubic in γ^2 , has a general validity for all the coupled systems that can be modeled with the equivalent circuit of Fig. 1, such as those in [26] and [27]. Equation (5) demonstrates that for $\omega_o = 1/(L_1C_1)^{1/2} = 1/(L_2C_2)^{1/2}$ the normalized frequency γ (which must be a real quantity) only depends on k and Q_2 . As expected, for $k = 0$ (uncoupled operation), (5) is fulfilled for $\gamma = \omega/\omega_o = 1$ only. From the inspection of (5), the variation of $f(\gamma, k, Q_2)$ versus k will be more significant for a larger Q_2 , since k becomes more relevant in the various coefficients. To understand this counterintuitive result, one must consider that though the external resonator is a series one, it enters the oscillator equations in a parallel manner. This is better seen by considering the Taylor series expansion of the coupled admittance Y_c about $k = 0$

$$Y_c(\omega, k) \cong \frac{1}{jL_1\omega} + \frac{k^2L_2}{L_1} \frac{1}{\frac{1}{jC_2\omega} + jL_2\omega + R_2}. \quad (6)$$

The form of (6) is that of a parallel connection of L_1 with a series resonator R_2, L_2, C_2 , affected by the factor k^2L_2/L_1 . Note that the approximation (6) has been introduced for illustration purposes only and will not be used in any of the calculations presented in this work. Fig. 2 presents the nomogram that provides γ versus k taking Q_2 as a parameter. For a Q_2 value higher than (approximately) 4 there are three real solutions, one departing from $\gamma = 1$ at $k = 0$ and the other two appearing from certain k and belonging to an isolated curve. The open curve departs from $\gamma = 1$ and decreases with k for reasons given later in this section. For a higher Q_2 the curve deviates from $\gamma = 1$ from a lower k . The additional solutions (in the disconnected curve) are due to changes of the slope of $Y_{c,i}(k, \omega)$ versus ω . This slope is positive (indicated with ‘‘P’’) in the open curve, negative (indicated with ‘‘N’’) in the lower section of the isolated curve, and positive in the upper section, so the change of slope takes place at the turning point. The k value from which the isolated curve arises decreases when increasing Q_2 .

Though in general only a rigorous stability analysis (based on pole-zero identification [28], for instance) can guarantee the fulfillment of the oscillation startup conditions, an admittance/impedance analysis can be helpful to facilitate these conditions at the design stage. In the circuit of Fig. 1, one should have $Y_{T,r}(V = 0, \omega_i(k), k) < 0$ at the frequencies $\omega_i(k)$, where i is an index, that fulfills $Y_{T,i}(\omega_i, k) = 0, \partial Y_{T,i}(\omega_i, k)/\partial \omega > 0$. The condition $Y_{T,r} < 0$ depends on the real part of (2), given by

$$Y_{c,r}(k, L_1, L_2, \omega) = \frac{L_1L_2C_2^2R_2k^2\omega^2}{C_2^2L_1^2L_2^2(k^2-1)^2\omega^4 + [C_2^2L_1^2R_2^2 + 2C_2L_2L_1^2(k^2-1)]\omega^2 + L_1^2}. \quad (7)$$

For each k , the function (7) tends to zero at $\omega = 0$ and $\omega \rightarrow \infty$, and exhibits a maximum at

$$\omega_{\max} = \frac{1}{\sqrt{(1-k^2)L_2C_2}}. \quad (8)$$

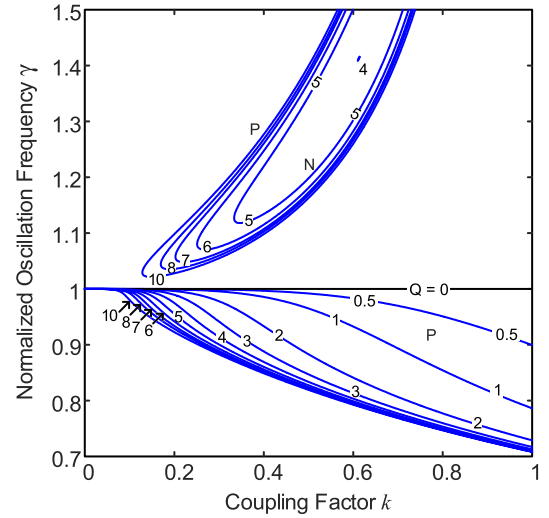


Fig. 2. Nomogram providing the variation of the normalized resonance frequency γ of the circuit in Fig. 1 versus the coupling factor k and taking Q_2 as a parameter. The usual condition $\omega_o = 1/(L_1C_1)^{1/2} = 1/(L_2C_2)^{1/2}$ is assumed.

Replacing (8) into (7), the maximum of the real part of the coupled admittance is

$$Y_{c,r}(\omega_{\max}, k) = \frac{L_2k^2}{L_1R_2}. \quad (9)$$

The maximum departs from zero at $k = 0$ (uncoupled conditions) and increases with k in a quadratic fashion. It increases with the ratio L_2/L_1 and decreases with R_2 .

The frequency ω_{\max} in (8) shifts to higher values when increasing k , as shown in Fig. 3(a), which presents the variation of $Y_{T,r} = a + Y_{c,r}$ in the circuit of Fig. 1 for different k and Q_2 values. The quality factor Q_2 has been modified by changing L_2 and calculating C_2 to maintain the same resonance frequency $C_2 = 1/(L_2\omega_o^2)$. In Fig. 3 when changing L_2 and C_2 , we have also modified the oscillator elements as $L_1 = L_2$ and $C_1 = C_2$.

Fig. 3(b) shows the variation of $Y_{T,i}(V = 0, \omega)$, which, for a larger Q_2 , exhibits a more significant variation versus k and a lower slope. Note that the frequency at which the imaginary part crosses through zero decreases with k in agreement with the nomogram in Fig. 2. This can be understood by paying attention to the frequency ω_c at which the function $Y_{c,i}(k, \omega)$ intersects with $-1/(L_1\omega)$, this being the termination admittance of the uncoupled oscillator. This intersection frequency is calculated imposing $Y_{c,i}(k, \omega) + 1/(L_1\omega) = 0$, which provides

$$\omega_c = \frac{1}{\sqrt{(1-k^2)L_2C_2}}. \quad (10)$$

It agrees with the one at which the real part $Y_{c,r}(k, \omega)$ takes its maximum value [see (8)]. One will have $Y_{c,i}(k, \omega) > -1/(L_1\omega)$ below ω_c , so for $\omega_c > \omega_o$, the startup frequency will shift from its original value ω_o to lower values since we are adding a less negative imaginary part to $C_1\omega$. The opposite is true for $\omega_c < \omega_o$. This explains the evolution of the open curves in Fig. 2. Fig. 3(c) presents the variation of both the real and imaginary parts of $Y_T(V = 0, \omega)$ for

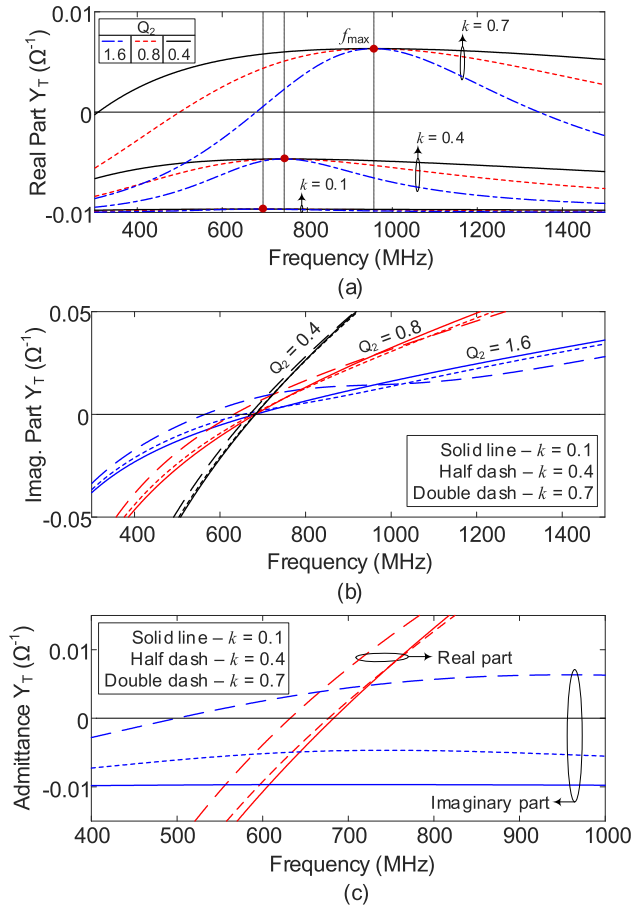


Fig. 3. Small-signal analysis. (a) Variation of $Y_{T,r}(V = 0, \omega)$ for different values of k and Q_2 . (b) Variation of $Y_{T,i}(V = 0, \omega)$. (c) Oscillation startup conditions for $Q_2 = 0.8$ and three different k values.

$Q_2 = 0.8$ and three different k values. As gathered from the figure, the oscillation conditions are not fulfilled from certain k , due to the increase in the maximum of $Y_{c,r}$. However, the shift to higher frequencies of this maximum, plus the evolution of the resonance frequencies predicted by the nomogram may give rise to a second oscillation interval, as shown in Section II-B.

B. Steady-State Oscillation

The steady-state oscillation amplitude is calculated by replacing the solutions of (5), given by $\omega_i(k) = \gamma_i(k)\omega_o$, into the following real equation:

$$\begin{aligned} Y_{T,r} &= a + \frac{3}{4}bV^2 + Y_{c,r}(\omega, k) \\ &= a + \frac{3}{4}bV^2 + \frac{Q_2^{-1}k^2\gamma^2/(L_1\omega_o)}{(k^2-1)^2\gamma^4 + [Q_2^{-2} + 2(k^2-1)]\gamma^2 + 1} = 0. \end{aligned} \quad (11)$$

As gathered from (10), the oscillation amplitude depends on γ and k , as well as ω_o and L_1 . Solving (11), the oscillation amplitude is

$$V = \sqrt{\frac{-Y_{c,r}(\omega_i(k), k) - a}{3b/4}}. \quad (12)$$

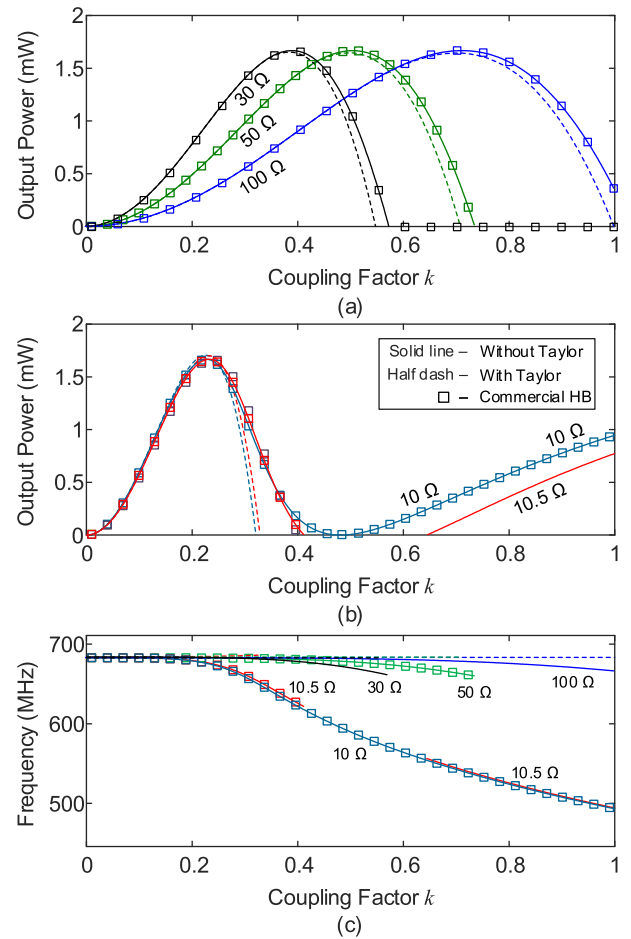


Fig. 4. Oscillator solution curve versus k for different values of R_2 . HB simulations with $NH = 1$ and seven harmonics are overlapped with the curves obtained with the new analytical formulation. (a) Output power for R_2 between 30Ω and 100Ω . (b) For $R_2 = 10 \Omega$ and 10.5Ω . (c) Frequency for R_2 between 10Ω and 100Ω .

Because $a < 0$, the higher $Y_{c,r}(\omega_i, k)$ (while fulfilling $Y_{c,r}(\omega_i(k), k) < -a$), the smaller the oscillation amplitude. The output power is given by

$$P_{out} = 2Y_{c,r}(\omega_i(k), k) \frac{(-Y_{c,r}(\omega_i(k), k) - a)}{3b}. \quad (13)$$

The maximum of (13) is obtained for $Y_{c,r}(\omega_i, k) = -a/2$ and is given by $P_{out,max} = a^2/6b$, which only depends on the nonlinear-device parameters. This is verified in Fig. 4(a) and (b), which present the variation of the output power and frequency versus k for different values of R_2 . Under a higher R_2 , one requires a higher k to obtain $Y_{c,r}(\omega_i, k) = -a/2$ and the oscillation is extinguished at a higher k , in agreement with the lower value of the conductance maximum in (9).

In Fig. 4(a) and (b) the results of the complete formulation are compared with those obtained with the approximation in [15] based on the use of a Taylor-series expansion in k . They are overlapped up to a certain k , but the approximation in [15] overestimates the k value at which the oscillation is extinguished. Unlike the approximate formulation, the complete one can predict the resurgence of the periodic oscillation curve for relatively low R_2 values. The variation of the oscillation frequency versus k is shown in Fig. 4(c).

In agreement with the nomogram of Fig. 2, when increasing k there is a progressive deviation from ω_o to lower values and this reduction is more significant for lower R_2 (higher Q_2). The new analytical formulation has been validated with HB simulations considering the fundamental frequency only and $NH = 7$ harmonic terms. Due to the high-quality factor of the oscillator, we obtain the same results in the two cases. These results are overlapped with those obtained with the analytical formulation. The HB results represented with squares for $R_2 = 50 \Omega$ and $R_2 = 10 \Omega$ are overlapped in Fig. 4. Note that to obtain the second oscillation curve for $R_2 = 10 \Omega$ an auxiliary generator (AG) [29], [30] was necessary to supply an initial guess to the default oscillator analysis in commercial HB. Otherwise, the commercial HB software failed to provide this solution that was missed in [15].

C. Oscillation Boundaries

At the oscillation boundaries, the oscillation condition is fulfilled for $V = 0$, which, in terms of γ and k (or any other parameter), provides the two real equations

$$\begin{aligned} Y_{T,r}(0, \gamma, k) &= a + \frac{Q_2^{-1} k^2 \gamma^2 / (L_1 \omega_o)}{(k^2 - 1)^2 \gamma^4 + [Q_2^{-2} + 2(k^2 - 1)] \gamma^2 + 1} = 0 \\ f(\gamma, k) &= (k^2 - 1)^2 \gamma^6 + [3(k^2 - 1) + Q_2^{-2}] \gamma^4 \\ &\quad + [3 - Q_2^{-2} - k^2] \gamma^2 - 1 = 0. \end{aligned} \quad (14)$$

It is interesting to note that the oscillation is extinguished for $Y_{c,r}(\omega_i, k) = -a$, which is twice the value that provides the maximum output power. Fig. 5(a) presents the contours of zero value of the two functions in (14) in the plane defined by γ and k for $R_2 = 50 \Omega$ and $R_2 = 10.5 \Omega$. For $R_2 = 10.5 \Omega$, there are two intersection points at which the oscillation is extinguished or generated. Note that under the approximation in [15], there is no possibility to obtain more than one intersection. Fig. 5(b) presents the locus of points fulfilling (14) (Hopf locus [31]–[33]) traced in the plane defined by k and R_2 . The coupled system oscillates in the white and lined regions. The lined region is delimited by subcritical Hopf bifurcations, so the generated oscillation curve exhibits a turning point (see the inset). As expected, the oscillation interval with regular behavior versus k increases with R_2 . Note that the coupling effects would become negligible for too large R_2 .

D. Modulated Behavior

The recent work [19] proposes the use of load-shift-keying modulation to transmit data from the external resonator to the oscillator; the resonator load is varied using a switch that gives rise to a modulation of the oscillation amplitude. Here advantage will be taken of the previous static formulation to predict the impact of R_2 . Fig. 6(a) presents the variation of the oscillation amplitude versus R_2 for different k values. In agreement with the previous derivations, there is an R_2 interval in which the oscillation is extinguished from a certain k [see Fig. 5(b)]. Under the modulation of R_2 , the circuit

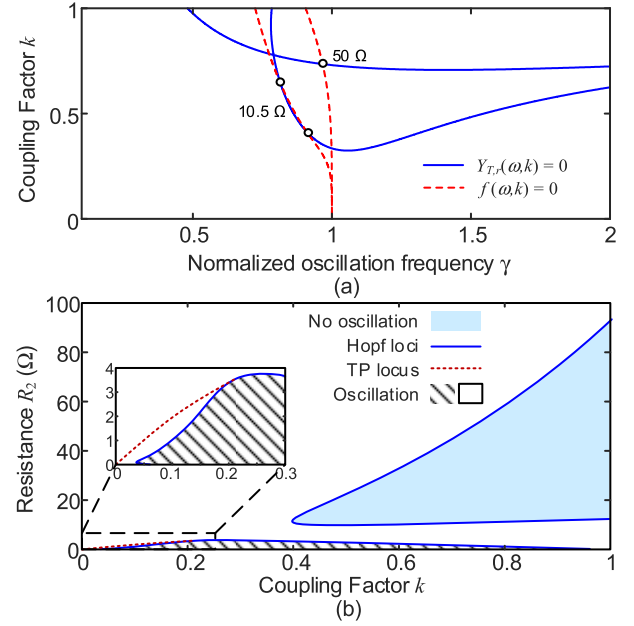


Fig. 5. Hopf-bifurcation loci. (a) Contours of zero value of the two functions in (14) in the plane defined by γ and k , for $R_2 = 50 \Omega$ and $R_2 = 10.5 \Omega$. (b) Hopf loci. The system oscillates in the white and lined regions.

is governed by the following system of envelope-domain equations at the fundamental frequency:

$$\begin{aligned} I(V(t)) + jC_1\omega V(t) + C_1\dot{V}(t) + I_1(t) &= 0 \\ -V(t) + jL_1\omega I_1(t) + L_1\dot{I}_1(t) + jM\omega I_2 + M\dot{I}_2(t) &= 0 \\ -V_2 + jL_2\omega I_2(t) + L_2\dot{I}_2(t) + jM\omega I_1(t) + M\dot{I}_1(t) &= 0 \\ jC_1\omega V_3(t) + C_1\dot{V}_3(t) - I_2(t) &= 0 \\ V_2(t) + V_3(t) + R_2(t)I_2(t) &= 0 \end{aligned} \quad (15)$$

where $M = k(L_1L_2)^{1/2}$ and the variables $V(t)$, $V_2(t)$, $V_3(t)$, $I_1(t)$, and $I_2(t)$ are the time-varying phasors at the fundamental frequency ω of the voltages v , v_2 , v_3 and currents i_1 , i_2 , indicated in the circuit of Fig. 1.

The coupling will give rise to dynamical effects at the envelope scale, $M\dot{I}_1(t)$, $M\dot{I}_2(t)$, which will be stronger for a higher k . Note that system (15) accounts for the changes in the oscillation frequency in the time variation of the phase of the state variables through the integral $\int \Delta\omega(t)dt$, so a sufficiently fine time step must be used to take this phase variation into account. For proper operation, the oscillation must exhibit sufficient sensitivity to the resistor R_2 in the expected k range. We have considered a periodic change between 50Ω and 5Ω (close to the loss resistor of a switch), with the period $T = 25 \mu s$, with the results shown in Fig. 6(b). For the higher k values (0.4 and 0.5), there is an oscillation extinction. The startup time after the extinction is highly dependent on k , as expected from (15). In fact, for higher k , the system dominant poles at $R_2 = 50 \Omega$ are closer to the imaginary axis, as shown in the pole locus of Fig. 7(a), obtained through pole-zero identification [28] that are traced versus k . At $k = 0.5$, the poles are closer to the imaginary axis than at $k = 0.4$, which gives rise to a slower startup transient, as validated through time-domain integration in Fig. 7(b).

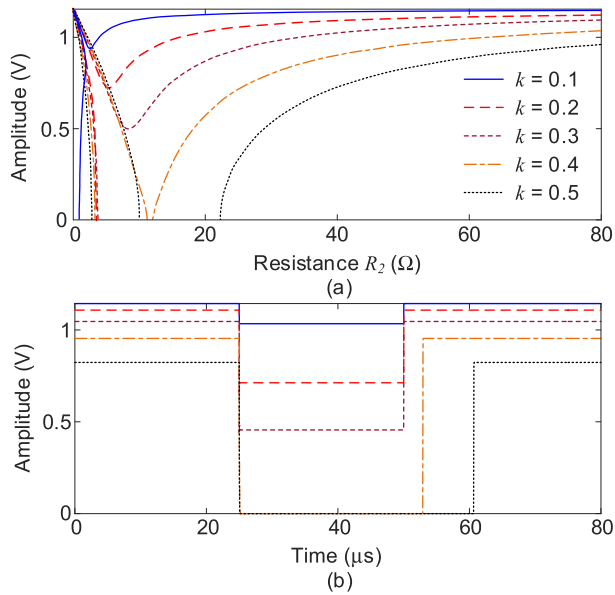


Fig. 6. Modulated behavior. (a) Variation of the oscillation amplitude versus R_2 in static conditions for different k . (b) Amplitude modulation when changing R_2 between 50Ω and 5Ω .

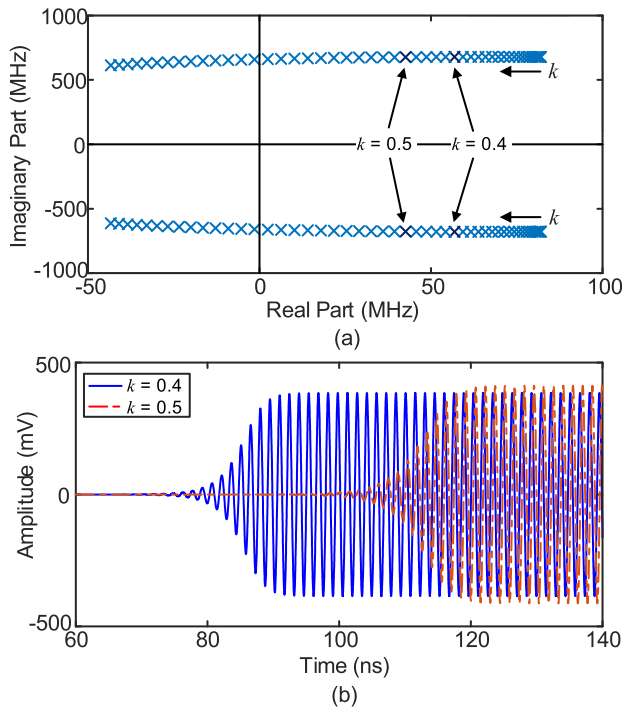


Fig. 7. Dependence of the startup transient on the coupling factor k . (a) Pole locus for $R_2 = 50 \Omega$. (b) Oscillation startup for $k = 0.4$ and $k = 0.5$.

III. ANALYSIS OF TRANSISTOR-BASED OSCILLATOR

The main analysis strategies presented in Section II will be applied to the Class-E oscillator in Fig. 8, based on the transistor MOSFET IRLML0040TRPbF (FR-4 substrate, $h = 1.6$ mm, $\epsilon_r = 4.5$). This proof-of-concept oscillator with no specific application operates at 12 MHz and is coupled to a series resonator, in a manner similar to [34]–[36]. The oscillator has been obtained by introducing series feedback in a Class-E amplifier through the procedure described in detail in [15]. With respect to the previous work [15], the

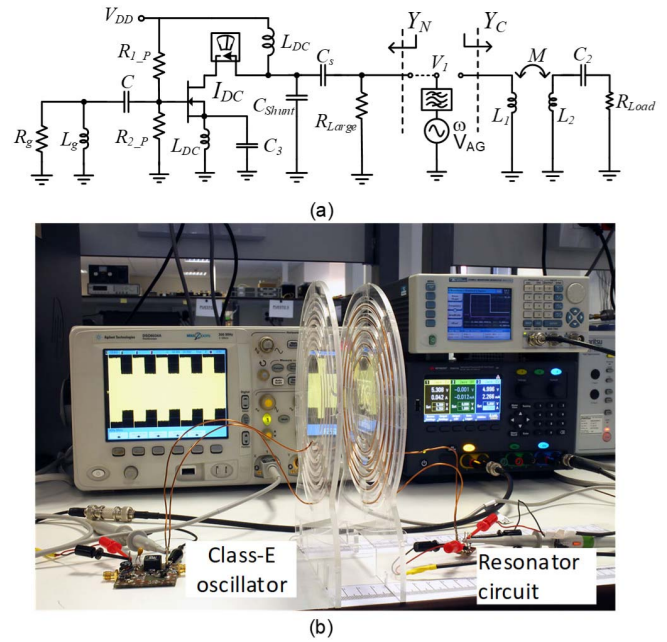


Fig. 8. Class-E oscillator at 12 MHz. (a) Schematic showing the connection of the AG to extract the nonlinear admittance function $Y_N(V, \omega)$ through HB. Note that Y_C is suppressed for this calculation. (b) Experimental setup.

aim here will be to reduce the k value from which a high transfer efficiency is obtained and maximize the k interval with this high efficiency. As stated, this is necessary even at short distances since there can be misalignments between the coils. We have modified the original amplifier design to obtain a higher efficiency under a smaller conductance in parallel, like the one resulting from a small k . This is immediately derived from (6). Under a small k , the resonance of the inductor and capacitor will ideally agree with the oscillation frequency and the equivalent admittance of the coupled circuit, looking into the oscillator inductor, will be

$$Y_c(\omega, k) \cong \frac{1}{jL_1\omega} + \frac{k^2 L_2}{L_1} \frac{1}{R_2}. \quad (16)$$

Thus, under a small k , the coupling effects introduce a high resistor in parallel. For an input voltage of 2.5 V and a parallel resistor of 1 k Ω (to emulate the coupling under small k), with the original values $C_1 = 100$ pF and $L_1 = 3.3$ μH , one obtains the efficiency of 19.82%. With the new values $C_1 = 70$ pF and $L_1 = 2.9$ μH , one obtains 47.65%. As will be shown, a penalty is the oscillation extinction for lower k values (in agreement with the results of Section II), which will be corrected through a suitable redesign of the coupled resonator.

Although the coupled admittance seen from the oscillator inductor is the same considered in Section II, one can expect some qualitative differences; this is because both the real part and imaginary parts of the nonlinear admittance function Y_N seen from the circuit output [see Fig. 8(a)] depend on the excitation frequency and voltage amplitude. In a small signal, the frequency variation of the imaginary part of this admittance will be more complex than that of the simple capacitive admittance of Section II.

A. Oscillation Startup

Although, as stated, only a rigorous stability analysis can reliably predict the oscillation startup, the admittance-based analysis is insightful from a design viewpoint. Moreover, it is a convenient way to relate these startup conditions with the loading effects of the inductively coupled resonator. To analyze the small-signal resonances, we will obtain the small-signal admittance function $Y_N(V = 0, \omega)$ exhibited by the oscillator from the terminals of its coupled inductor, as shown in Fig. 8(a). This function will be extracted from a commercial simulation software and added to the passive admittance $Y_c(k, \omega)$ of the coupled load (including the oscillator inductor) to evaluate the startup conditions [37]. The resonance condition is (17), as shown at the bottom of the next page

For given values of the oscillator inductor L_1 and external-resonator elements, (17) defines a resonance curve in the plane k, ω . This is easily obtained by performing a double sweep in k, ω and tracing the zero-value contour of $Y_{T,i}(0, \omega, k)$. When considering different values of R_2 , one gets the curve family in Fig. 9(a). All the curves $Y_{T,i}(0, \omega, k) = 0$ depart at $k = 0$ from the oscillation startup frequency in uncoupled conditions, denoted by ω_s , which in the oscillator of Fig. 8 is $f_s = 12.69$ MHz. It is also interesting to note that all the resonance curves intersect at the same k value ($k_o = 0.488$), regardless of R_2 , and the intersection frequency agrees with Ω_s [see Fig. 9(a)]. As shown in the following, this is because there is a k value for which the function $Y_{T,i}(0, \omega, k) = Y_{N,i}(0, \omega) + Y_{c,i}(\omega, k)$ formally agrees with the one obtained in uncoupled conditions and given by $Y_{T,i}(0, \omega, k = 0) = Y_{N,i}(0, \omega) - 1/(L_1\omega)$. Equating the two functions (which should be individually equal to zero) one obtains the condition

$$\frac{\left(L_1 L_2^2 C_2^2 (1 - k^2) \omega^5 + [L_1 C_2^2 R_2^2 + L_1 L_2 C_2 (k^2 - 2)] \omega^3 + L_1 \omega \right)}{\left(L_1 L_2^2 C_2^2 (k^2 - 1)^2 \omega^5 + [L_1 C_2^2 R_2^2 + 2L_1 L_2 C_2 (k^2 - 1)] \omega^3 + L_1 \omega \right)} = 1 \quad (18)$$

which is fulfilled at two points, both having $\omega = \omega_s$. The two k values are $k = 0$ and

$$k_o^2 = 1 - \frac{1}{C_2 L_2 \omega^2} \quad (19)$$

which is independent of R_2 . It is also independent of the numerical function $Y_{N,i}(0, \omega)$. Note that in the cubic-nonlinear oscillator considered in Section II, the startup frequency is $\omega_s = 1/(L_1 C_1)^{1/2} = 1/(L_2 C_2)^{1/2}$, so the only solution of (18) is $k_o = 0$. The value of k_o is relevant for the behavior of the coupled oscillator since it indicates a change in the startup frequency, from $\omega > \omega_s$ to $\omega < \omega_s$, or the opposite. In Fig. 9(a), for $R_2 < 100 \Omega$, the resonance curve $Y_{T,i}(0, \omega, k) = 0$ is multivalued with two turning points. In principle, the oscillation startup requires $Y_{T,r}(0, \omega_s, k) < 0$, $\partial Y_{T,i}(0, \omega_s, k)/\partial \omega > 0$ [38], which is fulfilled in the upper and lower sections of the curve, as indicated with ‘‘P.’’ As in the derivations of Section II, the multivalued section starts from a higher k as R_2 increases, and there is also a compression of

the resonance curve. At $R_2 \cong 85 \Omega$, the two turning points merge and the curve becomes single valued.

For a simple evaluation of the startup conditions, one can also trace the contour $Y_{T,r}(0, \omega_s, k) = 0$ in the plane defined by k and ω . This has been done in Fig. 9(b) and (c) for the two resistor values $R_2 = 50 \Omega$ and $R_2 = 100 \Omega$, respectively. In principle, the oscillation will startup in sections of the curve $Y_{T,i}(0, \omega_s, k) = 0$ with a positive slope, belonging to the region $Y_{T,r}(0, \omega_s, k) < 0$. On the other hand, the intersection points of the two curves $Y_{T,r}(0, \omega_s, k) = 0$ and $Y_{T,i}(0, \omega_s, k) = 0$ accurately provide the Hopf bifurcations at which the steady-state oscillation is generated or extinguished.

For a given function $Y_N(V = 0, \omega)$, the new graphical procedure enables a quick global evaluation of the oscillation startup conditions in terms of k and the element values of the external resonator. In the oscillator of Fig. 8, for $R_2 = 50 \Omega$, the startup conditions are fulfilled in two different sections of the resonance curve, at quite distinct frequencies. Increasing k from a low value, and moving along the resonance curve, the first oscillation will be extinguished at the Hopf bifurcation (H_1) obtained for $k = 0.465$ and the second oscillation will be generated at the Hopf bifurcation (H_2) obtained for $k = 0.609$. In contrast, for $R_2 = 100 \Omega$, the oscillation startup conditions are only fulfilled in one section, so a single oscillation curve is expected. This curve will be extinguished at the Hopf bifurcation point obtained for $k = 0.412$.

The results of Fig. 9 are validated in Fig. 10, which presents the real and imaginary parts of the total admittance function for $R_2 = 50 \Omega$ in standalone operation and three k values. For $k = 0.2$, the resonance curve is not multivalued, and the oscillation startup conditions are fulfilled at a frequency higher than the one in standalone operation, given by ω_s . In agreement with the derivations in Section II, this is because the crossing frequency that fulfills $Y_{c,i}(k, \omega_c) = -1/(L_1 \omega_c)$ is lower than ω_s . For $k = 0.45$, we are close to the limit of the fulfillment of the oscillation startup conditions at the upper-frequency range [H_1 in Fig. 9(b)] and for $k = 0.7$ the startup conditions are only fulfilled at the lower ω range. Thus, a qualitative change of the oscillation frequency to lower values can be expected.

B. Steady-State Oscillation

To obtain the steady-state oscillation curve versus k in an efficient and insightful manner, we will extract the nonlinear numerical admittance function $Y_N(V, \omega)$ from HB software. This is calculated by looking into the oscillator circuit from the coupled inductor terminals, as shown in Fig. 8. It is obtained by means of an HB simulation with the aid of an AG, also shown in Fig. 8, and as many harmonic terms as desired. A double sweep is carried out in ω and V , obtaining, at each sweep step, the function $Y_N(V, \omega)$ as the ratio between the AG current (pointing toward the oscillator circuit) and the AG voltage. The function $Y_N(V, \omega)$ is exported to in-house software, where it is combined with the analytical expression of $Y_c(k, \omega)$. From the same double sweep in commercial HB, one obtains also the oscillator drain current, given by $I_{DC}(V, \omega)$, which will allow the calculation of the power

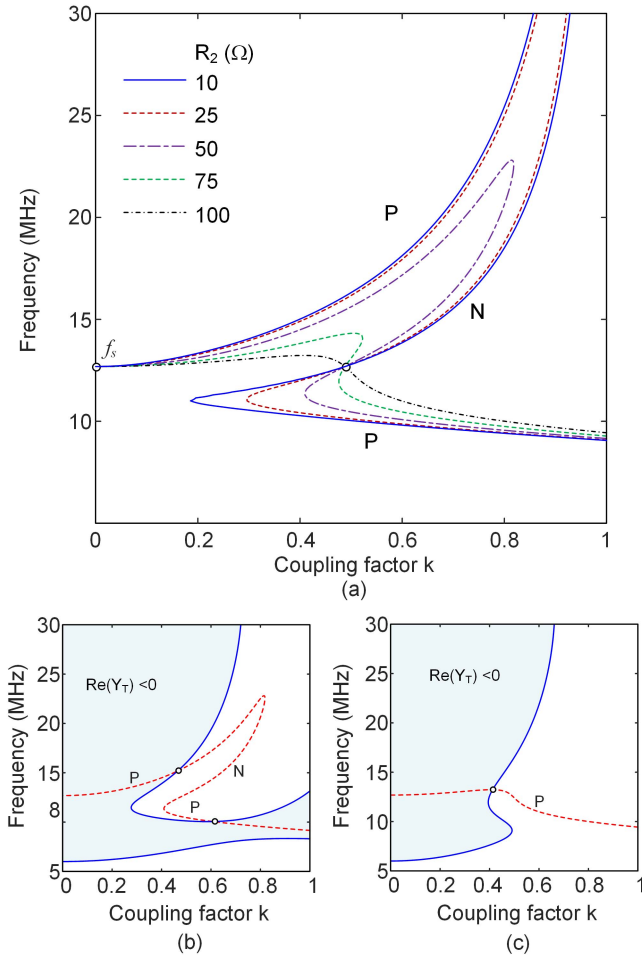


Fig. 9. New graphical method for a global evaluation of the oscillation startup conditions. (a) Family of zero-value contours of the function $Y_{T,i}(0, \omega, k)$ resulting from the variation of R_2 . All the curves intersect at the same point given by (19). (b) Resonance curve $Y_{T,i}(0, \omega, k) = 0$ and negative conductance boundary $Y_{T,r}(0, \omega_s, k) = 0$ for $R_2 = 50 \Omega$. The oscillation should startup in sections of $Y_{T,i}(0, \omega_s, k) = 0$ with positive slope that fulfills $Y_{T,r}(0, \omega_s, k) < 0$. The intersection points of $Y_{T,r}(0, \omega_s, k) = 0$ and $Y_{T,i}(0, \omega_s, k) = 0$ accurately provide the Hopf bifurcations. (c) Same for $R_2 = 100 \Omega$.

efficiency. The oscillation condition is (20), as shown at the bottom of the next page.

For each value of the external-resonator parameter (which may be k or a passive element value), one performs a sweep in ω and uses the numerical function $Y_N(V, \omega)$ to obtain two surfaces: $Y_{T,r}(V, \omega)$ and $Y_{T,i}(V, \omega)$, in the spaces defined by V, ω , and $Y_{T,r}$, and V, ω , and $Y_{T,i}$, respectively. Then, one obtains the zero-value contours $Y_{T,r}(V, \omega) = 0$ and $Y_{T,i}(V, \omega) = 0$ from the intersections of these surfaces with their respective zero-value planes. Finally, all the solutions of (20) coexisting for the particular parameter value are obtained from the intersections of the two zero-value contours $Y_{T,r}(V, \omega) = 0$ and $Y_{T,i}(V, \omega) = 0$. One should emphasize

that for each parameter value, there can be one or more intersection points V_o, ω_o , so the possibly multivalued solution curves are obtained in a straightforward manner, with no need for continuation procedures. The output power and drain efficiency are calculated interpolating the following functions at the solution points resulting from the intersections:

$$\begin{aligned} P_{\text{out}} &= \frac{1}{2} Y_{c,r}(k, \omega) V^2 \\ \eta_{\text{DC}} &= P_{\text{out}} / [V_{\text{DC}} I_{\text{DC}}(V, \omega)]. \end{aligned} \quad (21)$$

The solutions obtained with the described method are shown in Fig. 11. Even though the equations in (20) are formulated at the fundamental frequency, it is possible to predict the coupled-oscillator behavior with great accuracy. This is because the outer-tier function $Y_N(V, \omega)$ is extracted by means of an HB simulation with a sufficiently high number of harmonic terms ($NH = 7$ is considered here), which duly accounts for the strong nonlinearity of the transistor operation. Note that the oscillator equations (20) are written at the oscillator output node, where the harmonic content should be significantly filtered due to the parallel capacitor; the much higher harmonic content at the transistor terminals is considered in the HB calculation of $Y_N(V, \omega)$. The advantage of this numerical-analytical (N-A) procedure is its versatility versus changes in the coupled inductor and the external resonator. Under changes in k , the coupled inductor L_1 or the coupled resonator elements, only the two equations in (20) are solved in terms of V and ω , instead of performing a new HB oscillator analysis, often unable to complete the solution curves.

In Fig. 11, the results of (20) are compared with those provided by the default oscillation analysis of commercial HB, which confirms the existence of two distinct oscillation curves at different frequencies. In the first curve, the results of the new method and those provided by commercial HB are overlapped. However, in the second curve (for which several convergence problems were encountered in HB), there are discrepancies due to the significant reduction of the oscillation frequency [see Fig. 11(c)], and, as a result, of the filtering effects of the oscillator output capacitor. This has been validated with a second simulation in commercial HB, with the same number of harmonic terms ($NH = 7$) but using an ideal filter to remove the coupling effects at frequencies higher than the fundamental one. In that case, the results of the new method and those provided by commercial HB are overlapped. When increasing k , the accuracy of (20) will degrade if there is a strong reduction of the oscillation frequency; this is due to the impact of the resonator coupling at the harmonic terms. However, that undesired frequency variation can be predicted and mitigated with the resonance analysis in Fig. 9. Without that strong variation, the analysis based on (20) is fully applicable.

The extinction of the oscillation from relatively small k will give rise to unreliable behavior, since it establishes a

$$Y_{T,i}(0, \omega, k) = Y_{N,i}(0, \omega) - \frac{L_1 L_2^2 C_2^2 (1 - k^2) \omega^5 + [L_1 C_2^2 R_2^2 + L_1 L_2 C_2 (k^2 - 2)] \omega^3 + L_1 \omega}{\left[\frac{L_1 L_2^2 C_2^2 (k^2 - 1)^2 \omega^5 + [L_1 C_2^2 R_2^2 + 2 L_1 L_2 C_2 (k^2 - 1)] \omega^3 + L_1 \omega}{L_1 \omega} \right]} = 0 \quad (17)$$

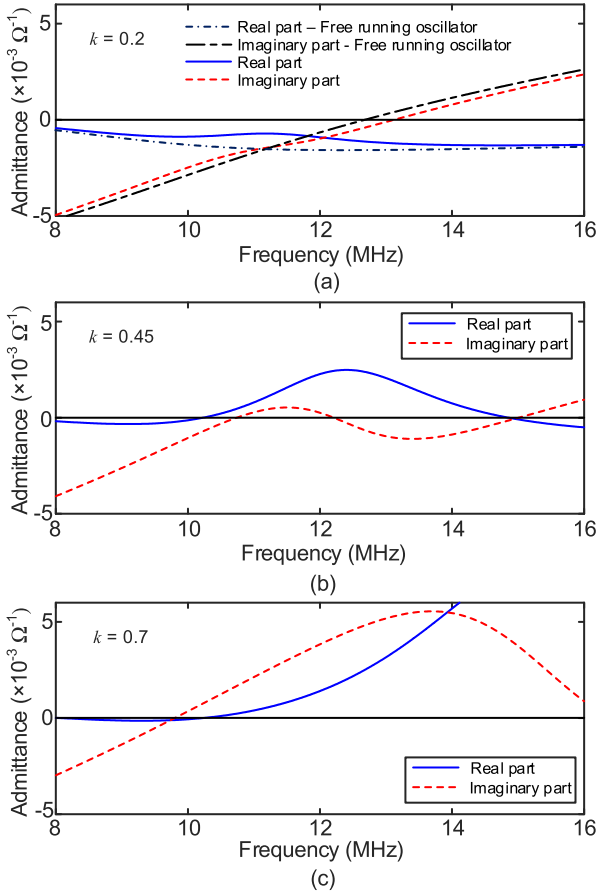


Fig. 10. Oscillation startup conditions in standalone operation and for three different k values. (a) $k = 0.2$. The coupling gives rise to an upward shift of the startup frequency. (b) $k = 0.45$. The startup conditions are fulfilled near the bifurcation that gives rise to the oscillation extinction. (c) $k = 0.7$. The startup conditions are fulfilled in the lower frequency range.

minimum operating distance between the oscillator and the resonator. On the other hand, the significant change in the oscillation frequency versus k , seen in Fig. 11(c), may lead the system to operate outside the regulated frequency bands. In view of the analytical study of Section II, in order to prevent the strong variation of the oscillation frequency, one should increase the quality factor of the full oscillator system,

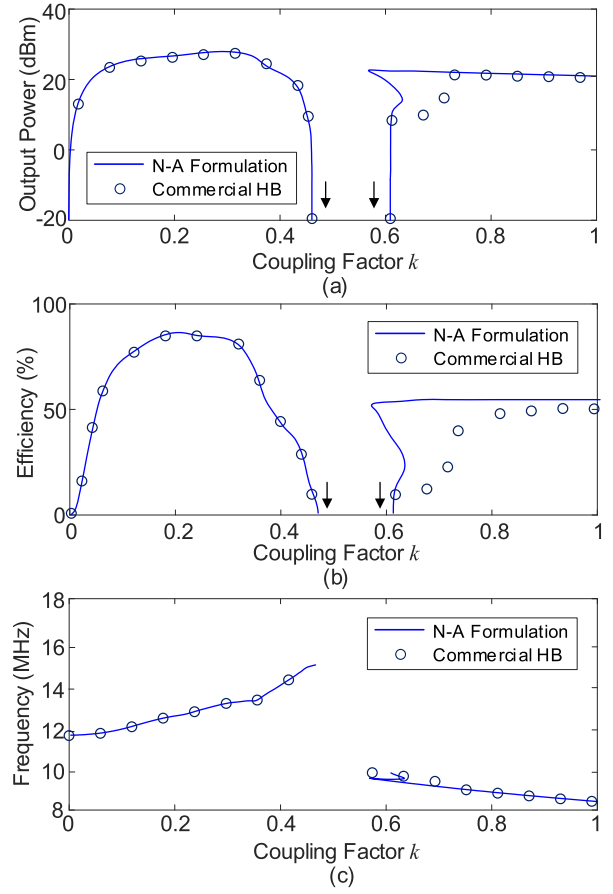


Fig. 11. Class-E oscillator coupled to a resonator with $R_2 = 50 \Omega$. Solution curves versus the coupling factor k , obtained with the N-A method and validated through HB with $NH = 7$. (a) Output power. (b) Efficiency. (c) Oscillation frequency.

or equivalently, reduce the quality factor Q_2 of the external oscillator. At a fixed resonance frequency ω_o , this can be done by increasing the output resistor R_2 or reducing the ratio L_2/C_2 , while maintaining the original resonance ω_{o2} of the external resonator. Here these modifications will be carried out without altering the original oscillator design, that is, keeping the original values of L_1 and the rest of its elements and parameters.

$$\begin{aligned}
 Y_{T,r}(V, \omega, k) &= Y_{N,r}(V, \omega) + \frac{L_1 L_2 C_2^2 R_2 k^2 \omega^4}{\left[L_1 L_2^2 C_2^2 (k^2 - 1)^2 \omega^5 + [L_1 C_2^2 R_2^2 + 2L_1 L_2 C_2 (k^2 - 1)] \omega^3 + L_1 \omega \right] L_1 \omega} = 0 \\
 Y_{T,i}(V, \omega, k) &= Y_{N,i}(V, \omega) - \frac{L_1 L_2^2 C_2^2 (1 - k^2) \omega^5 + [L_1 C_2^2 R_2^2 + L_1 L_2 C_2 (k^2 - 2)] \omega^3 + L_1 \omega}{\left[L_1 L_2^2 C_2^2 (k^2 - 1)^2 \omega^5 + [L_1 C_2^2 R_2^2 + 2L_1 L_2 C_2 (k^2 - 1)] \omega^3 + L_1 \omega \right] L_1 \omega} = 0
 \end{aligned} \quad (20)$$

$$\begin{aligned}
 Y_{T,r}(V, \omega, k) &= Y_{N,r}(V, \omega) + \frac{L_1 \omega_{o2}^{-2} C_2 R_2 k^2 \omega^4}{\left[L_1 \omega_{o2}^{-4} (k^2 - 1)^2 \omega^5 + [L_1 C_2^2 R_2^2 + 2L_1 \omega_{o2}^{-2} (k^2 - 1)] \omega^3 + L_1 \omega \right] L_1 \omega} = 0 \\
 Y_{T,i}(V, \omega, k) &= Y_{N,i}(V, \omega) - \frac{L_1 \omega_{o2}^{-4} (1 - k^2) \omega^5 + [L_1 C_2^2 R_2^2 + L_1 \omega_{o2}^{-2} (k^2 - 2)] \omega^3 + L_1 \omega}{\left[L_1 \omega_{o2}^{-4} (k^2 - 1)^2 \omega^5 + [L_1 C_2^2 R_2^2 + 2L_1 \omega_{o2}^{-2} (k^2 - 1)] \omega^3 + L_1 \omega \right] L_1 \omega} = 0
 \end{aligned} \quad (22)$$

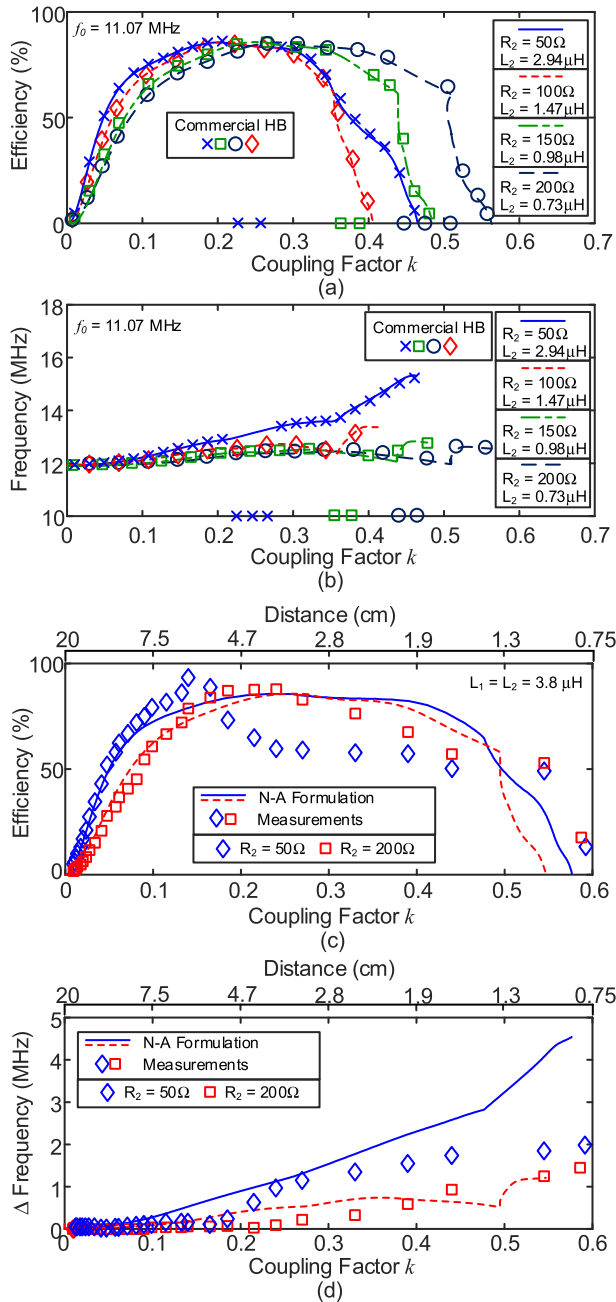


Fig. 12. Class-E oscillator. Influence of the external resonator design. (a) Efficiency for four different values of $\beta = C_2 R_2$, achieved by modifying R_2 and the pair L_2, C_2 . Solution curves obtained with commercial HB are superimposed. Note that this HB analysis failed to convergence in some intervals. (b) Oscillation frequency versus k for the same cases. (c) Power efficiency. New N-A method and experimental results for $R_2 = 50 \Omega$ and $R_2 = 200 \Omega$. (d) Frequency increment for the same cases ($R_2 = 50 \Omega$ and $R_2 = 200 \Omega$).

Because we will keep ω_{o2} at a constant value, we can write $L_2 = 1/(C_2 \omega_{o2}^2)$ and replace this expression in the steady-state oscillation equations (20), (22), as shown at the bottom of the previous page.

From inspection of the equation (22), under the condition $L_2 = 1/(C_2 \omega_{o2}^2)$, one can merge C_2 and R_2 into a single parameter $\beta = C_2 R_2$ since they only appear in the product $C_2 R_2$. Thus, provided that β has the same value, the solution curves obtained under modification of either R_2 or the pair L_2 and C_2 will be the same. This is verified in Fig. 12(a) and (b),

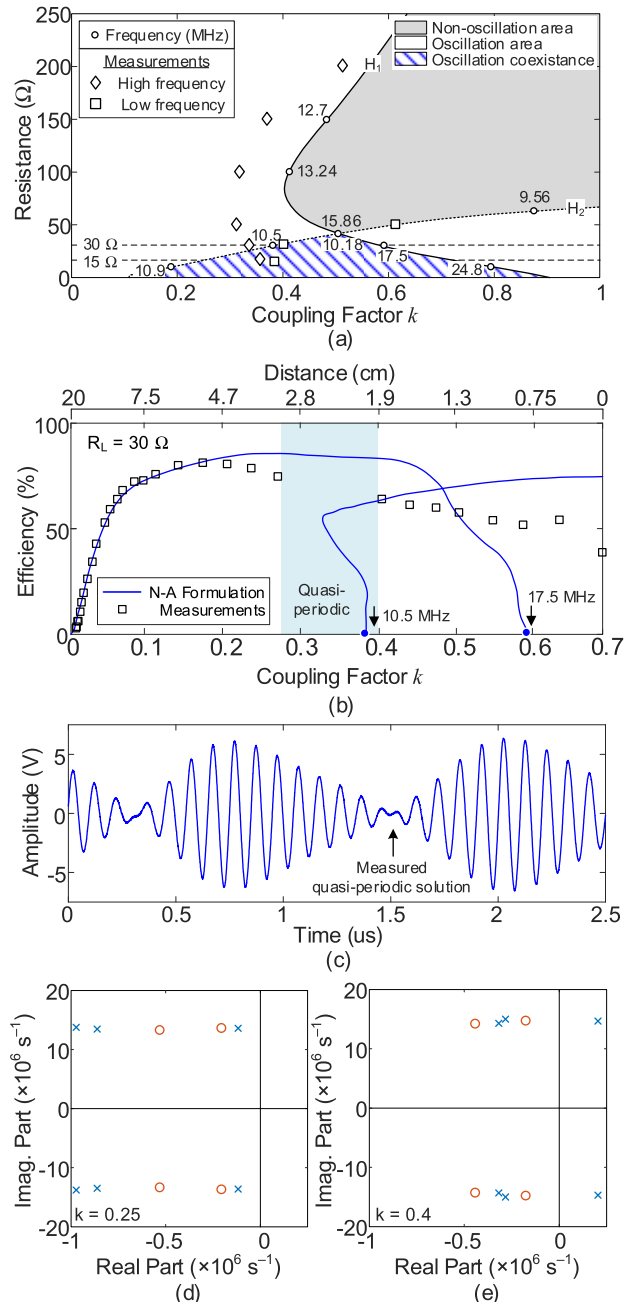


Fig. 13. Complex dynamics in the Class-E oscillator. (a) Hopf bifurcation loci in the plane defined by k and R_2 . Measurement points are superimposed. The interval with experimental quasi-periodic behavior is indicated. (b) Solution curves (N-A method) in the region with coexistence of oscillations. (c) Experimental quasi-periodic solution obtained for $R_2 = 30 \Omega$ and $k = 0.4$. (d) and (e) Pole-zero identification demonstrating the existence of secondary Hopf bifurcations in the periodic solution curve at ω_n .

which present the variations of the power-transfer efficiency and the oscillation frequency versus k for four distinct β values, each achieved by modifying R_2 and by modifying the pair L_2, C_2 . The curves obtained for the same β are overlapped. Results obtained with HB simulations in these two different manners are superimposed and demonstrate the equivalence. Note that in some k intervals, the HB oscillator analysis failed to converge. We must emphasize that an identical response versus k does not imply the same behavior when varying the distance between the inductors. This is because the coupling

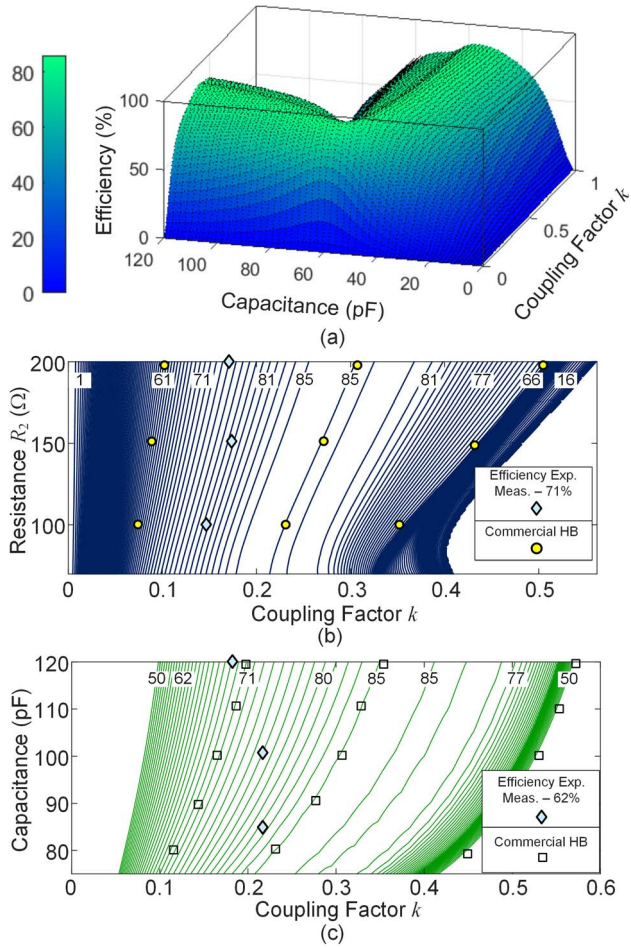


Fig. 14. Steady-state oscillation surface. (a) Surface obtained in terms of the power efficiency versus C_2 and k . (b) Constant efficiency contours in the plane defined by R_2 and k . The results have been validated at specific points with commercial HB, superimposed in the figure, and with measurements. (c) Constant efficiency contours in the plane defined by C_2 and k . HB simulations and measurements are also shown.

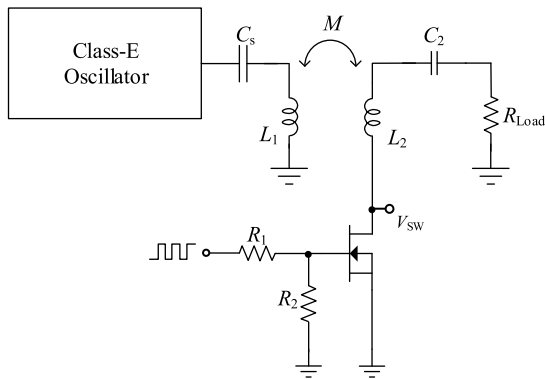


Fig. 15. Introduction of switch in the oscillator of Fig. 8 to implement a load shift keying modulation. The switch is based on the same MOSFET used for the oscillator design.

factor k depends on the geometry of L_2 , and, for the same distance, one can expect a smaller k for a lower L_2 , as this will imply a smaller diameter and/or number of turns [39]. Thus, for the same efficiency, the coils will have to be closer. Nevertheless, the possibility to reduce L_2 can have interest in certain applications [5].

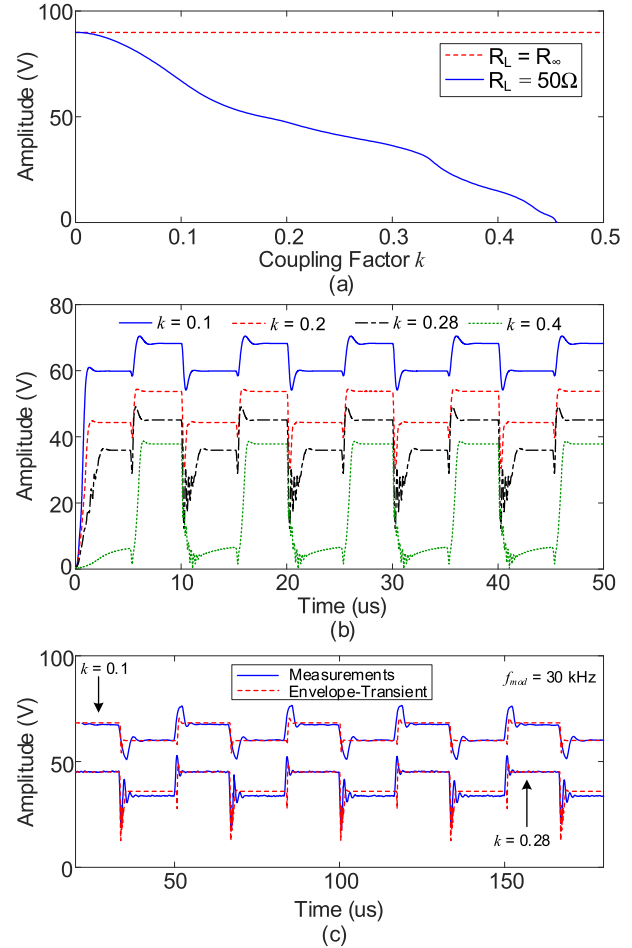


Fig. 16. Class-E oscillator under a load shift keying modulation. (a) Variation of the oscillation amplitude versus k in the two cases $R_2 = 50 \Omega$ and $R_2 = R_\infty$. (b) Oscillation amplitude under a rectangular modulation signal of period $T = 33.3 \mu s$ and different values of the coupling factor k . (c) Validation with experimental results for two k values.

As seen in Fig. 12(a), the parameter β has a strong impact on the coupled oscillator response versus k and can be optimized to broaden the k interval with high efficiency. When increasing β , there is a reduction of the variation of the oscillation frequency versus k [see Fig. 12(b)]. Fig. 12(c) and (d) present the experimental results obtained for $R_2 = 50 \Omega$ and $R_2 = 200 \Omega$. The k factor of the coils has been estimated versus the distance from the measurement of the scattering parameters under variations of this distance. Taking into account the results of this characterization, in Fig. 12(c) and (d), we have introduced a second horizontal axis with the distance between the coils. The measurement points are displayed at the distances at which they were carried out. For the larger R_2 , the oscillation is preserved up to a larger distance. However, a shorter distance is needed to get a high efficiency, in agreement with the analytical study of Section II. For $R_2 = 200 \Omega$, there is an excellent correspondence with the measurement results. The discrepancies for $R_2 = 50 \Omega$ are attributed to modeling inaccuracies in the presence of a stronger frequency variation.

C. Oscillation Boundaries

The oscillation boundaries in the plane defined by k and R_2 [or k and C_2 , under the condition $L_2 = 1/(C_2\omega_0^2)$] can

be efficiently determined by tracing the Hopf-bifurcation loci. At each Hopf bifurcation, the oscillation condition is fulfilled at a small signal, so the calculation of the Hopf loci will be carried out using the small-signal function $Y_N(V = 0, \omega)$, extracted from the commercial simulation software. Due to the equivalence of the results obtained when varying R_2 or C_2 , only one of the two (R_2) will be considered in the calculation of the loci. The resistor R_2 will be swept solving, at each R_2 step, the following system in terms of k and ω (23), as shown at the bottom of the page:

In practice, the system (23) is solved by performing, for each R_2 , a double sweep in k and ω [within the interval considered in $Y_N(V = 0, \omega)$] and obtaining the intersections of the zero value contours of the two surfaces $Y_{T,r}(0, \omega, k)$ and $Y_{T,i}(0, \omega, k)$. This provides the two distinct Hopf loci, shown in Fig. 13(a), at which the higher-frequency and lower-frequency oscillations are extinguished or generated when varying k at a constant R_2 .

One Hopf locus (H_1) is composed of the points at which the higher frequency oscillation at ω_h is extinguished when increasing k . The second Hopf locus (H_2) is composed of the points at which the lower frequency oscillation at ω_l is generated when increasing k . Above the intersection point between the two loci [see Fig. 13(a)], at $k = 0.505$ and $R_2 = 42 \Omega$, there is a k interval in which the dc solution is stable. Below the intersection point, the solution curve at ω_l is generated before the curve at ω_h is extinguished, as seen in Fig. 13(b), obtained with (20). Below the intersection point, the oscillation at ω_l arises from an unstable dc solution, so at least the initial section of the periodic oscillation curve at ω_l should be unstable [29], [40]–[42]. However, and because the oscillation at ω_l is stable in the upper k interval, this curve at ω_l must undergo a secondary-inverse Hopf bifurcation [40] at a particular k . This implies the existence of a stable quasi-periodic solution with two incommensurate fundamental frequencies, corresponding to those of the two detected oscillations [30]. That quasi-periodic solution is generated from the curve at ω_h , as shown in Fig. 13(d) and (e), corresponding to $R_2 = 30 \Omega$. The two-pole loci, obtained by applying pole-zero identification to the solution at ω_h , imply a crossing through the imaginary axis (when increasing k) of a pair of complex conjugate poles at a frequency close to ω_l .

The waveform measured for $k = 0.4$ is shown in Fig. 13(c). Even above the intersection point, in the R_2 interval for which there are two Hopf bifurcations H_1 and H_2 , the observation of the stable dc solutions might be difficult if secondary Hopf bifurcations keep taking place in the periodic oscillation curve at ω_h . This quasi-periodic solution would be extinguished in a secondary-inverse Hopf bifurcation in the curve at ω_l .

Thus, the quasi-periodic curve (not calculated here, due to its lack of interest) constitutes a “bridge” between the two distinct periodic solutions. The discussed complex dynamics is a result of the multi-resonance behavior of the coupled oscillator under a low R_2 shown in Fig. 9. The investigation presented here warns about several undesired phenomena that may be encountered in these conditions.

D. Constant Efficiency Contours

One advantage of the efficient calculation of the steady-state oscillation curves through the numerical-analytical formulation in (20) is the possibility to obtain a steady-state oscillation surface in the plane defined by k and an arbitrary parameter η , belonging to the external resonator. As gathered from the previous comparisons with HB (under $NH = 7$ harmonic terms), the surface will be accurate unless there is a significant reduction of the oscillation frequency when increasing k , leading to a reduction of the filtering effects of the output capacitor of the Class-E oscillator (and thus to a higher impact of the second harmonic term). Even in the worst cases, this will only occur from a relatively large k , as shown in the previous analyses. On the other hand, this strong frequency variation is undesired and should be avoided in the system design.

The oscillation surface will be obtained by performing a double sweep in η and k and calculating, at each sweep step, the steady-state oscillatory solution and its efficiency through (19) and (20). The oscillation surface traced in terms of the power efficiency versus k and $\eta = C_2$ is shown in Fig. 14(a). Obtaining this surface took 3 min and 21 s in an Intel¹ Core i7 6700 (sixth generation) Quad-Core CPU (16 GB RAM). To the best of our knowledge, this is the first time that such an oscillation surface is calculated; moreover, it has been obtained for a circuit of significant complexity. The examination of this surface is very meaningful and reveals that for the lower C_2 values, the oscillation persists for all k , but the resulting efficiency is much lower than the one achieved in Fig. 12. Thus, the new procedure enables a global evaluation of the behavior of the coupled-oscillator circuit versus the coupling factor.

Once the oscillation surface is available, one can easily obtain constant-efficiency contours in the plane defined by k and the chosen parameter η . This will allow a straightforward determination of the variation of the transfer efficiency versus k for any η value. Fig. 14(b) and (c) present the constant efficiency contours traced in the planes defined by R_2 and k and C_2 and k , respectively. In the two cases, the results

¹Registered trademark.

$$\begin{aligned}
 Y_{T,r}(0, \omega, k) &= Y_{N,r}(0, \omega) + \frac{L_1 L_2 C_2^2 R_2 k^2 \omega^4}{\left[L_1 L_2^2 C_2^2 (k^2 - 1)^2 \omega^5 + [L_1 C_2^2 R_2^2 + 2L_1 L_2 C_2 (k^2 - 1)] \omega^3 + L_1 \omega \right] L_1 \omega} = 0 \\
 Y_{T,i}(0, \omega, k) &= Y_{N,i}(0, \omega) - \frac{L_1 L_2^2 C_2^2 (1 - k^2) \omega^5 + [L_1 C_2^2 R_2^2 + L_1 L_2 C_2 (k^2 - 2)] \omega^3 + L_1 \omega}{\left[L_1 L_2^2 C_2^2 (k^2 - 1)^2 \omega^5 + [L_1 C_2^2 R_2^2 + 2L_1 L_2 C_2 (k^2 - 1)] \omega^3 + L_1 \omega \right] L_1 \omega} = 0
 \end{aligned} \tag{23}$$

have been validated at specific points with commercial HB, superimposed in the figure, and with measurements.

E. Modulated Behavior

Modulation of the oscillation signal can be carried out through the time variation of R_2 [19], which would demand a rectifier and baseband circuitry that have not been implemented in this work. For the modulation, we have considered two values: a $50\ \Omega$ load and a large resistance R_∞ , which is achieved with the aid of the switch shown in Fig. 15, implemented with the same MOSFET used for the oscillator design. Fig. 16(a) presents the (static) variation of the oscillation amplitude versus k obtained in the two cases: $R_2 = 50\ \Omega$ and $R_2 = R_\infty$. In agreement with the results of Section II, the sensitivity to R_2 decreases with k . The effect of the R_2 modulation on the oscillatory solution has been analyzed with envelope transient [21]–[23]. To initialize the oscillation of the homogeneous system, we have connected a small-signal current source, which is disconnected from the circuit with the aid of an ideal filter after a few time steps. The frequency of this source agrees with the one obtained in unmodulated conditions for $R_2 = 50\ \Omega$. Fig. 16(b) presents the envelope of the oscillation signal under a rectangular modulation with the period $T = 33.3\ \mu\text{s}$ and different values of the coupling factor k . In Fig. 16(c), the results are successfully compared with experimental measurements for two k values. Because R_2 switches between $50\ \Omega$ and a large value, the modulation frequency cannot be too high. Note that this is just a proof of concept, since the main contribution of the work is the investigation of the system performance and the variety of analysis tools, which can be applied to oscillators with different topologies and goals.

IV. CONCLUSION

An in-depth analytical study of the behavior of an oscillator coupled to an external resonator has been presented. The investigation departs from the case of a cubic-nonlinearity oscillator and focuses on the effect of the coupled resonator on the oscillation amplitude and frequency. Criteria to minimize the variation of the oscillation frequency, which may lead to operating outside the regulated bands, and maximize the interval with a high-power transfer efficiency are provided. The results of this initial investigation have been extended to a practical Class-E power oscillator. A new insightful and easy-to-use graphical method has been presented to detect the evolution of the resonance frequencies versus the coupling factor. It allows predicting the regions of oscillation startup as well as their variation with the external resonator quality factor. The steady-state oscillation analysis has been carried out through an analytical-numerical methodology based on the extraction of the nonlinear admittance function that describes the active core from the resonator. It enables a versatile analysis under variations in the coupling factor and any element value of the coupled resonator. Several phenomena have been demonstrated such as the oscillation extinction and new onset when increasing the coupling factor and the possible existence of stable quasi-periodic solutions.

REFERENCES

- [1] J. Garnica, R. A. Chinga, and J. Lin, "Wireless power transmission: From far field to near field," *Proc. IEEE*, vol. 101, no. 6, pp. 1321–1331, Jun. 2013.
- [2] S. R. Khan, S. K. Pavuluri, and M. P. Y. Desmulliez, "Accurate modeling of coil inductance for near-field wireless power transfer," *IEEE Trans. Microw. Theory Techn.*, vol. 66, no. 9, pp. 4158–4169, Sep. 2018.
- [3] S. Liu, M. Liu, S. Yang, C. Ma, and X. Zhu, "A novel design methodology for high-efficiency current-mode and voltage-mode class-E power amplifiers in wireless power transfer systems," *IEEE Trans. Power Electron.*, vol. 32, no. 6, pp. 4514–4523, Jun. 2017.
- [4] M. Liu, S. Liu, and C. Ma, "A high-efficiency/output power and low-noise megahertz wireless power transfer system over a wide range of mutual inductance," *IEEE Trans. Microw. Theory Techn.*, vol. 65, no. 11, pp. 4317–4325, Nov. 2017.
- [5] M. O. Abouzeid and A. Tekin, "Adaptive 6.78-MHz ISM band wireless charging for small form factor receivers," in *Proc. IEEE Int. Symp. Circuits Syst. (ISCAS)*, May 2017, pp. 1–4.
- [6] Q. Ma, M. R. Haider, S. Yuan, and S. K. Islam, "Power-oscillator based high efficiency inductive power-link for transcutaneous power transmission," in *Proc. 53rd IEEE Int. Midwest Symp. Circuits Syst.*, Aug. 2010, pp. 537–540.
- [7] A. Järndal and T. Petrovic, "GaN-based oscillators for wireless power transfer applications," in *Proc. Int. Conf. Adv. Comput. Telecommun. (ICACAT)*, Dec. 2018, pp. 1–5.
- [8] R. L. O. Pinto, R. M. Duarte, F. R. Sousa, I. Müller, and V. J. Brusamarello, "Efficiency modeling of class-E power oscillators for wireless energy transfer," in *Proc. IEEE Int. Instrum. Meas. Technol. Conf. (I2MTC)*, May 2013, pp. 271–275.
- [9] D. Rattanasungam, K. Phaebua, and T. Lertwiriyaprapa, "Power control unit for E-class power oscillator of 6.78 MHz wireless power transfer," in *Proc. Int. Symp. Antennas Propag. (ISAP)*, Oct. 2017, pp. 1–2.
- [10] Y. Yamashita and K. Wada, "Wireless power transmitter using parallel-tuned class-E power oscillator," in *Proc. Int. Symp. Electron. Smart Devices (ISESD)*, Oct. 2017, pp. 287–290.
- [11] S. Liu, M. Liu, M. Fu, C. Ma, and X. Zhu, "A high-efficiency class-E power amplifier with wide-range load in WPT systems," in *Proc. IEEE Wireless Power Transf. Conf. (WPTC)*, May 2015, pp. 1–3.
- [12] H.-M. Hsu and J.-K. Liao, "An extensive load resistor operation of wireless power transfer system in 13.56 MHz resonant mode," in *Proc. Asia-Pacific Microw. Conf. (APMC)*, Nov. 2018, pp. 1411–1413.
- [13] A. N. Laskovski and M. R. Yuze, "Class-E oscillators as wireless power transmitters for biomedical implants," in *Proc. 3rd Int. Symp. Appl. Sci. Biomed. Commun. Technol. (ISABEL)*, Nov. 2010, pp. 1–5, doi: [10.1109/ISABEL.2010.5702913](https://doi.org/10.1109/ISABEL.2010.5702913).
- [14] A. Costanzo, M. Dionigi, F. Mastri, and M. Mongiardo, "Rigorous modeling of mid-range wireless power transfer systems based on royer oscillators," in *Proc. IEEE Wireless Power Transf. (WPT)*, May 2013, pp. 69–72.
- [15] V. Ardila, F. Ramirez, and A. Suarez, "Nonlinear analysis of a high-power oscillator inductively coupled to an external resonator," *IEEE Microw. Wireless Compon. Lett.*, vol. 31, no. 6, pp. 737–740, Jun. 2021.
- [16] O. Abdelatty, X. Wang, and A. Mortazawi, "Position-insensitive wireless power transfer based on nonlinear resonant circuits," *IEEE Trans. Microw. Theory Techn.*, vol. 67, no. 9, pp. 3844–3855, Sep. 2019.
- [17] P. R. Troyk and G. A. DeMichele, "Inductively-coupled power and data link for neural prostheses using a class-E oscillator and FSK modulation," in *Proc. 25th Annu. Int. Conf. IEEE Eng. Med. Biol. Soc.*, vol. 4, Sep. 2003, pp. 3376–3379.
- [18] Q. Ma, M. R. Haider, and S. K. Islam, "A high efficiency inductive power link and backward telemetry for biomedical applications," in *Proc. IEEE Sensors*, Nov. 2010, pp. 89–93.
- [19] A. Yousefi, A. A. Abidi, and D. Markovic, "Analysis and design of a robust, low-power, inductively coupled LSK data link," *IEEE J. Solid-State Circuits*, vol. 55, no. 9, pp. 2583–2596, Sep. 2020.
- [20] T.-C. Yu and C.-L. Yang, "Design and analysis of dual-frequency power amplifier for wireless power and data transfer application," in *Proc. IEEE Wireless Power Transf. Conf. (WPTC)*, May 2017, pp. 1–4.
- [21] J. Roychowdhury, "Efficient methods for simulating highly nonlinear multi-rate circuits," in *Proc. 34th Annu. Conf. Design Autom. Conf. (DAC)*, Jun. 1997, pp. 269–274, doi: [10.1145/266021.266092](https://doi.org/10.1145/266021.266092).
- [22] E. Ngoya and R. Larcheveque, "Envelope transient analysis: A new method for the transient and steady state analysis of microwave communication circuits and systems," in *IEEE MTT-S Int. Microw. Symp. Dig.*, vol. 3, Jun. 1996, pp. 1365–1368, doi: [10.1109/MWSYM.1996.512189](https://doi.org/10.1109/MWSYM.1996.512189).

- [23] H. G. Brachtendorf, G. Welsch, and R. Laur, "A time-frequency algorithm for the simulation of the initial transient response of oscillators," in *Proc. IEEE Int. Symp. Circuits Syst. (ISCAS)*, vol. 6, May/Jun. 1998, pp. 236–238, doi: [10.1109/ISCAS.1998.705255](https://doi.org/10.1109/ISCAS.1998.705255).
- [24] L. Gustafsson, G. H. B. Hansson, and K. I. Lundstrom, "On the use of describing functions in the study of nonlinear active microwave circuits," *IEEE Trans. Microw. Theory Techn.*, vol. 20, no. 6, pp. 402–409, Jun. 1972.
- [25] A. De Angelis *et al.*, "Resonant inductive wireless power transfer links operating in a coupling-independent regime: Theory and experiments," in *Proc. IEEE Int. Instrum. Meas. Technol. Conf. (I2MTC)*, May 2017, pp. 1–6.
- [26] J. C. F. A. de Casaleiro, L. A. B. G. Oliveira, and I. M. Filanovsky, "Active coupling RC-oscillator," in *Quadrature RC-Oscillators (Analog Circuits and Signal Processing)*. Cham, Switzerland: Springer, 2019, pp. 69–90.
- [27] I. Dumitrescu, S. Bachir, D. Cordeau, J.-M. Paillot, and M. Iordache, "Modeling and characterization of oscillator circuits by van der pol model using parameter estimation," *J. Circuits, Syst. Comput.*, vol. 21, no. 5, Aug. 2012, Art. no. 1250043.
- [28] J.-M. Collantes *et al.*, "Pole-zero identification: Unveiling the critical dynamics of microwave circuits beyond stability analysis," *IEEE Microw. Mag.*, vol. 20, no. 7, pp. 36–54, Jul. 2019.
- [29] F. Ramirez, M. Ponton, S. Sancho, and A. Suarez, "Stability analysis of oscillation modes in quadruple-push and Rucker's oscillators," *IEEE Trans. Microw. Theory Techn.*, vol. 56, no. 11, pp. 2648–2661, Nov. 2008.
- [30] F. Ramirez, S. Sancho, and A. Suárez, "Oscillation modes in multiresonant oscillator circuits," *IEEE Trans. Microw. Theory Techn.*, vol. 64, no. 12, pp. 4660–4675, Dec. 2016.
- [31] A. Suarez, F. Ramirez, and S. Sancho, "Generalized stability criteria for power amplifiers under mismatch effects," *IEEE Trans. Microw. Theory Techn.*, vol. 63, no. 12, pp. 4415–4428, Dec. 2015.
- [32] A. Suarez and F. Ramirez, "Stability and bifurcation analysis of multi-element non-foster networks," *IEEE Trans. Microw. Theory Techn.*, vol. 66, no. 4, pp. 1817–1830, Apr. 2018.
- [33] A. Suarez, F. Ramirez, and S. Sancho, "Stability analysis of power amplifiers under output mismatch effects," *IEEE Trans. Microw. Theory Techn.*, vol. 62, no. 10, pp. 2273–2289, Oct. 2014.
- [34] K. O. Gurov, "Study of a class e power amplifier tuning effect on output power and efficiency of an inductive wireless power transfer system," in *Proc. IEEE Conf. Russian Young Researchers Electr. Electron. Eng. (ElConRus)*, Jan. 2021, pp. 2803–2807.
- [35] E. V. Selyutina and E. A. Mindubaev, "Effects of class e power amplifier parameters on output power of inductive wireless power transfer system with capacitive tuning," in *Proc. IEEE Conf. Russian Young Researchers Electr. Electron. Eng. (ElConRus)*, Jan. 2021, pp. 2874–2878.
- [36] W.-T. Chen, R. A. Chinga, S. Yoshida, J. Lin, and C.-K. Hsu, "A 36 W wireless power transfer system with 82% efficiency for LED lighting applications," *Trans. Jpn. Inst. Electron. Packag.*, vol. 6, no. 1, pp. 32–37, 2013.
- [37] A. Suarez, R. Melville, and F. Ramirez, "Analysis and synthesis of hysteresis loops in an oscillator frequency characteristic," *IEEE Trans. Microw. Theory Techn.*, vol. 67, no. 12, pp. 4890–4904, Dec. 2019.
- [38] K. Kurokawa, "Some basic characteristics of broadband negative resistance oscillator circuits," *Bell Syst. Tech. J.*, vol. 48, no. 6, pp. 1937–1955, Jul. 1969.
- [39] S. Raju, R. Wu, M. Chan, and C. P. Yue, "Modeling of mutual coupling between planar inductors in wireless power applications," *IEEE Trans. Power Electron.*, vol. 29, no. 1, pp. 481–490, Jan. 2014.
- [40] H. Kawakami, "Bifurcation of periodic responses in forced dynamic nonlinear circuits: Computation of bifurcation values of the system parameters," *IEEE Trans. Circuits Syst.*, vol. 31, no. 3, pp. 248–260, Mar. 1984.
- [41] A. Suárez, *Analysis and Design of Autonomous Microwave Circuits*. Hoboken, NJ, USA: Wiley, 2008.
- [42] A. Suarez, "Check the stability: Stability analysis methods for microwave circuits," *IEEE Microw. Mag.*, vol. 16, no. 5, pp. 69–90, Jun. 2015.



Victor Ardila (Student Member, IEEE) was born in Bucaramanga, Santander, Colombia. He received the professional career degree in mechatronic engineering from the Autonomous University of Bucaramanga (UNAB), Santander, in 2013, and the M.E. degree from the University of Málaga (UMA), Andalucía, Spain, in 2017. He is currently pursuing the Ph.D. degree in information technology and communications in mobile networks at the University of Cantabria (UC), Santander, Spain.

His research interests include the design and analysis of non-linear circuits and RF/microwave systems.



Franco Ramírez (Senior Member, IEEE) received the Licentiate degree in electronic systems engineering from the Military School of Engineering (EMI), La Paz, Bolivia, in 2000, and the Ph.D. degree in communications engineering from the University of Cantabria, Santander, Spain, in 2005.

From 1999 to 2000, he worked with Ericsson de Bolivia Telecomunicaciones, La Paz, where he was involved in projects related to global system for mobile communications (GSM) and time division multiple access (TDMA) technologies.

From 2009 to 2013, he was a Research Fellow of the "Ramón y Cajal" Program, funded by the Spanish Ministry of Science and Innovation, at the Communications Engineering Department, University of Cantabria, where he is currently an Associate Professor. His research interests include phase noise, stability, and the development of nonlinear techniques for the analysis and design of autonomous microwave circuits.



Almudena Suárez (Fellow, IEEE) was born in Santander, Spain. She received the Licentiate degree in electronic physics and the Ph.D. degree from the University of Cantabria, Santander, Spain, in 1987 and 1992, respectively, and the Ph.D. degree in electronics from the University of Limoges, Limoges, France, in 1993.

She is currently a Full Professor at the University of Cantabria and the Head of the Microwave Engineering and Radiocommunication Systems Research Group. She has authored the book *Analysis and Design of Autonomous Microwave Circuits* (IEEE-Wiley, 2009) and coauthored the book *Stability Analysis of Nonlinear Microwave Circuits* (Artech House, 2003).

Prof. Suárez is a member of the Technical Committee of the IEEE International Microwave Symposium (IEEE MTT-S) and the European Microwave Week. She was a member of the Board of Directors of the European Microwave Association from 2012 to 2020, where she is also the Publication Officer. She was the Coordinator of the Communications and Electronic Technology Area for the Spanish National Evaluation and Foresight Agency (ANEP) from 2009 to 2013. She was the Chair of the 2014 and 2015 Editions of IEEE Topical Conference on RF/Microwave Power Amplifiers (PAWR), Newport Beach and San Diego. She was the General TPC Chair of European Microwave Week 2018. She was the Chair of the *IEEE Microwave Magazine* Best Paper Award Committee from 2017 to 2020. She was the Editor-in-Chief of the *International Journal of Microwave and Wireless Technologies* (Cambridge University Press journals) from 2013 to 2018. She is currently an Associate Editor of *IEEE Microwave Magazine* and IEEE TRANSACTIONS ON MICROWAVE THEORY AND TECHNIQUES. She was an IEEE Distinguished Microwave Lecturer from 2006 to 2008.